CLIMATOLOGY

Reduced tropical cyclone densities and ocean effects due to anthropogenic greenhouse warming

Jung-Eun Chu[1,2], Sun-Seon Lee[1,2]*, Axel Timmermann[1,2]*, Christian Wengel[1,2], Malte F. Stuecker[3], Ryohei Yamaguchi[1,2]

Tropical cyclones (TCs) are extreme storms that form over warm tropical oceans. Along their tracks, TCs mix up cold water, which can further affect their intensity. Because of the adoption of lower-resolution ocean models, previous modeling studies on the TC response to greenhouse warming underestimated such oceanic feedbacks. To address the robustness of TC projections in the presence of mesoscale air-sea interactions and complex coastal topography, we conduct greenhouse warming experiments using an ultrahigh-resolution Earth System Model. We find that a projected weakening of the rising branches of the summer Hadley cells suppresses future TC genesis and TC-generated ocean cooling. The forced response is similar to recent observational trends, indicating a possible emergence of the anthropogenic signal beyond natural variability levels. In the greenhouse warming simulations, landfalling TCs intensify, both in terms of wind speed and associated rainfall. Our modeling results provide relevant information for climate change adaptation efforts.

INTRODUCTION

Tropical cyclones (TCs) are one of the most fatal and costliest weather disasters on our planet. It is therefore of utmost importance to understand how their tracks, intensity, and associated rainfall patterns will change in response to greenhouse warming. A recent study (*1*) reveals consistent patterns in observed changes in TC occurrence and those simulated by anthropogenically forced climate models, leading to the conclusion that greenhouse warming may have already altered the statistics of TCs beyond the level of natural variability. However, there still remain major uncertainties in model-based projections of TCs, in part due to the effects of horizontal resolution (*2*, *3*), the representation of atmosphere-ocean coupling (*4*–*6*), the choice of physical parameterizations (*7*), and discretization of the underlying physical equations (*8*).

To determine the sensitivity of TC statistics and dynamics to radiative perturbations, three main dynamical modeling approaches have been adopted:

1) In "pseudo–global warming experiments," sea surface temperature (SST) boundary conditions for a high-resolution atmosphere general circulation model are obtained by adding SST responses from coarse-resolution coupled Earth system model projections onto the observed SST climatology (*9*–*13*). A key advantage of this method is that realistic observed SST conditions can be used for the control simulation. However, this approach ignores possible two-way interactions between atmosphere and ocean.

2) In fully coupled global Earth system model simulations, either the atmosphere, ocean, or both are run at horizontal resolutions that are suitable for representing mesoscale features (*3*, *14*, *15*). Even though this approach is computationally more intensive, it captures the interaction between TCs and the ocean more realistically. One disadvantage is that the coupled model SST climatology may still differ considerably in some regions from the observations. Such biases can influence the representation of TCs.

3) In regional atmosphere or coupled model experiments, coarse-resolution model simulations are used as lateral boundary conditions (*2*). One of the key disadvantages is that depending on the domain size, the dynamics inside the region of interest is controlled by a mixture of prescribed horizontal boundary conditions, external forcing, and internal dynamics. Oftentimes, the relative role of these factors is difficult to disentangle.

So far, most studies on future changes in global TC statistics rely on the pseudo–global warming setup (*9*–*13*) or on coupled models with relatively coarse-resolution ocean models (*3*, *14*) that use ~100-km horizontal resolution. Their main conclusions can be summarized as follows: Global warming is likely to increase the TC intensity (frequency ratio of strong versus weak events). Moreover, the thermodynamic enhancement of atmospheric moisture content is accompanied by a robust increase in TC-related precipitation (*3*, *11*, *14*). One of the remaining uncertainties is the expected change in the global number of TCs. Whereas most of the low-resolution global climate models and some SST-forced high-resolution atmosphere models project a general decline in the TC frequency (*11*, *12*), other higher-resolution models (up to ~50 km) and statistical/dynamical downscaling studies predict an increase (*2*). There is some evidence to suggest that the TC sensitivity in coupled models depends on the horizontal resolution (*3*), which underscores further the need to use high-resolution configurations in both atmosphere and ocean.

Resolving mesoscale oceanic features is important for TC sensitivity studies, because strong and slowly propagating TCs are known to enhance vertical ocean mixing, bringing colder subsurface waters to the surface and mixing warm surface waters down to several hundred meters. In some cases, after the passage of a TC, SST can rapidly decrease by up to 10°C around the area of maximum wind speed (*16*). Even though the affected area is small [O(20 to 100 km)], the surface temperature drop can provide an immediate negative feedback on the TC development (*5*). In contrast, a TC-generated and mixing-induced increase in upper ocean heat content (OHC) may be beneficial for the generation of subsequent TCs (*17*, *18*). It has further been suggested that TC-generated ocean mixing may play

[1]Center for Climate Physics, Institute for Basic Science (IBS), Busan 46241, South Korea. [2]Pusan National University, Busan 46241, South Korea. [3]Department of Oceanography and International Pacific Research Center, School of Ocean and Earth Science and Technology, University of Hawaiʻi at Mānoa, Honolulu, HI, USA.
*Corresponding author. Email: sunseonlee@pusan.ac.kr (S.-S.L.); axel@ibsclimate.org (A.T.)

an important role in the global transport of heat toward the poles (*19*). We therefore conclude that to properly quantify the sensitivity of TCs to greenhouse warming, a coupled modeling approach is necessary that is able to adequately resolve important TC characteristics, such as the eye of a TC and oceanic events (*20*), such as cold wakes, inertial currents, upper ocean mixing, and TC-generated mesoscale eddies.

Here, we present results from century-long present-day [PD; with a CO_2 concentration of 367 parts per million (ppm)], instantaneous CO_2 doubling (2×CO_2, 734 ppm) and CO_2 quadrupling (4×CO_2, 1468 ppm) climate sensitivity experiments conducted with the Community Earth System Model (CESM; version 1.2.2) (see Materials and Methods for model descriptions). The numerical simulations, which are among the highest-resolution coupled climate change experiments conducted so far, are based on the Community Atmosphere Model version 5 (CAM5) with an atmospheric horizontal resolution of 1/4° and the Parallel Ocean Program version 2 (POP2) ocean model with a nominal resolution of 1/10°. These resolutions are sufficient to resolve key mesoscale process, both in the atmosphere and ocean (*21*). Our study focuses on the simulated CO_2-induced changes in TC frequency, TC-related oceanic wakes, translation speed, and landfall characteristics.

RESULTS

CESM ultrahigh-resolution simulations

The PD simulation was integrated for 140 years, and the 2×CO_2 and 4×CO_2 experiments are 100 years long. In response to instantaneous CO_2 doubling and quadrupling, global mean surface air temperatures increase toward the end of the simulations by 2.5° and 5.1°C (fig. S1A), whereas ocean temperatures increase by 1.8° and 3.8°C. The top of the atmosphere (TOA) radiation imbalance reduces from around 1 to 0.2 W m^{-2} in the PD experiment (fig. S1B). Initially, there is a large radiation imbalance in response to greenhouse gas forcing, but it weakens gradually to around 1 W m^{-2} in the 2×CO_2 and 2 W m^{-2} in the 4×CO_2 experiments, indicating that the coupled system slowly approaches near-equilibrium conditions. However, we emphasize that a complete equilibration would take up to several hundred years. Global mean precipitation averaged over the last 20 years of the simulations increases by 3.8 and 7.1% for 2×CO_2 and 4×CO_2 experiments relative to the PD climatology (fig. S1C).

Compared with lower-resolution Earth system models, the ultrahigh-resolution PD experiment shows substantial improvements in the representation of SST and precipitation (figs. S2 and S3) (*21*). Areas of substantial improvement relative to the coarse-resolution CESM version (*21*) include the California and Humboldt Current Systems (fig. S2), where a more realistic representation of orography and alongshore winds in combination with the 1/10° ocean model resolution translates to an improved simulation of coastal upwelling processes, stratus clouds (*22*), and air-sea coupling. In other areas, such as the western tropical Pacific (warm bias) and tropical Atlantic (cold bias), improvements are less obvious (*21*, *23*). In tropical regions, SST biases are tightly connected with precipitation biases. A more realistic representation of SST in PD also leads to an improvement in large-scale precipitation patterns, in particular the eastern tropical Pacific Intertropical Convergence Zone (ITCZ) (fig. S3). Our simulations show a considerable reduction in the double-ITCZ problem, which is commonly found not only in coarse-resolution (*24–26*) but also in some high-resolution coupled models (*22*, *27*).

Although the simulated ITCZ is still too intense and the meridional extent of the convergence zone is too narrow in PD [likely due to excessive low-level convergence (*7*)], its overall structure resembles the TRMM satellite observations (*28*) reasonably well. Furthermore, our PD simulation exhibits a more realistic representation of regional precipitation over major storm track regions, the East Asian summer monsoon, and along steep topographic gradients, such as the foothills of the Himalayas (fig. S3).

Owing to the high 1/10° horizontal resolution of POP2, our simulations resolve mesoscale oceanic eddy activity in good qualitative agreement with observational altimetric estimates (fig. S4). Maxima in daily sea surface height variability are found in the main western boundary current regions and the Antarctic Circumpolar Current. Compared with the AVISO altimeter data, our simulations tend to overestimate eddy activity in the extratropics while showing weaker variability in the tropics (fig. S4C).

TC genesis location and tracks

Our TC analysis focuses on the last 20 years of each simulation (PD, CO_2 doubling, and CO_2 quadrupling). To identify genesis locations and tracks of TCs, we use instantaneous six-hourly surface pressure, 10-m wind speed, and surface vorticity data, as well as cutoff criteria, which are similar to those used in recently developed algorithms (Materials and Methods) (*7*). Comparison of the PD simulation with the observed best track data from the International Best Track Archive for Climate Stewardship version 4 (IBTrACS4) (*29*) documents that the ultrahigh-resolution CESM captures the major genesis locations, tracks, and densities over the western North Pacific, North Atlantic, eastern Pacific, South Indian Ocean, and South Pacific reasonably well (Fig. 1). However, in terms of TC frequency, we find an underestimation in the model over the western North Pacific, eastern Pacific, and North Atlantic and an overestimation of activity over the central tropical Pacific near the dateline due to ITCZ biases, similar to what has been reported from previous high-resolution modeling studies (*7*, *11*, *21*). Despite these seasonally modulated biases, the model provides a reasonable representation of basin-scale climatologies in the Indian Ocean and the South Pacific (fig. S5), including the number of TCs per year, mean duration, travel distance, translation speed, and intensity (table S1).

In response to CO_2 doubling, the model simulates a decreased TC track density over almost the entire tropics and subtropics (with the exception of the eastern Bay of Bengal and patches in the Coral and Philippine Seas). This change resembles the observed trend in TC density (Fig. 1C), and the pattern similarity is consistent with the notion that greenhouse warming may have already started to alter the observed TC tracks and frequencies (*1*). In the 4×CO_2 experiment, the reduction in TC density is even more pronounced, extending further into the subtropics (Fig. 1E). TC track density decreases globally by 7 and 32% in the 2×CO_2 and 4×CO_2 experiments, respectively. This result is qualitatively consistent with previous studies using high-resolution (20- to 50-km) SST-forced pseudo–global warming simulations (*9–13*). However, we emphasize that there are still remaining modeling uncertainties in the projected response of global TC numbers. Other fully coupled modeling studies using, e.g., the HiFLOR setup (*3*), show no discernible response of global TC frequencies to increasing CO_2 concentrations but a decrease, when observed SSTs are nudged toward observations in the same model (*3*).
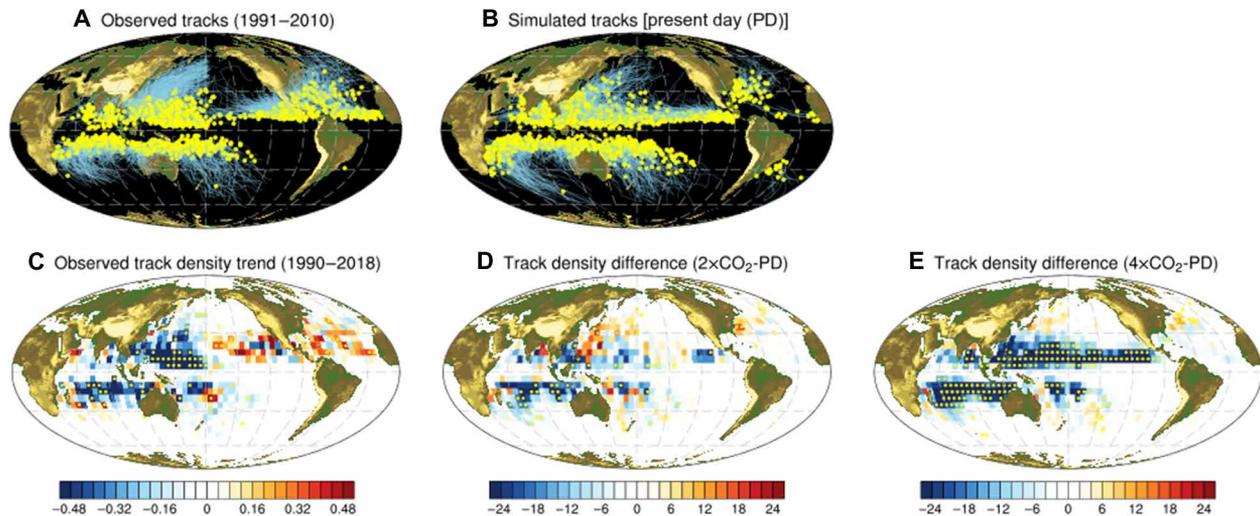
Fig. 1. PD and future TC genesis location and tracks. (**A** and **B**) TC genesis location (yellow dots) and tracks (blue lines) from (A) observations and (B) PD simulation. (**C**) Linear trend of the observed TC track density (hours per day per year) for the period 1990 to 2018. (**D** and **E**) Track density changes (hours per day) in (D) CO_2 doubling ($2\times CO_2$) and (E) CO_2 quadrupling ($4\times CO_2$) conditions related to PD condition. Observational data are from IBTrACS4 during the 1990 to 2018 period. Track density was obtained by the number of TC tracks over 5×5 degree grid box. Yellow dotted areas in (C) to (E) indicate values for which the local null hypothesis of zero relation can be rejected at the 95% level based on a Student's t test.

The reduction in TC density in parts of the tropics (Fig. 1, D and E) can be explained in terms of the simulated changes in relative humidity and vertical velocity (Fig. 2). Less favorable environmental conditions for TC genesis, in particular a reduction in relative humidity and anomalous downward atmospheric motion (Fig. 2A), can be linked to an overall weakening of the rising branches of the summer hemispheric Hadley cells (Fig. 2, B and C), in agreement with recent studies (30–32). Contrasting the TC suppression in the tropics, our CO_2 perturbation experiments simulate an increase in TC track densities at higher latitudes, namely, east of Japan and along the east coast of North America (Fig. 1, D and E). This feature is related to the overall expansion of the subtropics in response to greenhouse warming and the associated poleward shift of the storm tracks (33).

Given that extratropical TCs are typically characterized by higher translation speeds (34), an increase in extratropical TC density (Fig. 1, D and E) may also translate into an increase in averaged translation speeds. Our PD simulation captures the overall distribution of the translation speeds in good agreement with the observations (fig. S6A). However, the mean translation speed is slightly overestimated (table S1). In our simulations, we find an increase in the average translation speed by 2.1 and 10.9% in the $2\times CO_2$ and $4\times CO_2$ experiments, respectively. Furthermore, the probability distribution of translation speed also changes its shape, exhibiting a decrease in the number of slow-moving TCs and a marked increase in TCs with translation speeds >40 km hour^{-1} (fig. S6A). This shift of the distribution can be attributed to the increase in TC density poleward of 30°S and 30°N (fig. S6B) simulated in the $2\times CO_2$ and $4\times CO_2$ experiments.

Effect of air-sea coupling
TCs extract vast amounts of energy from the surface ocean in the form of sensible and latent heat fluxes that result from strong wind speeds. During the passage of a TC and when ocean mixed layers are relatively shallow, the surface ocean can cool considerably around the TC core due to the entrainment of deeper cold waters into the

mixed layer (35). The TC-induced local SST reduction, referred to as "cold wake," can further influence the development and life cycle of TCs. Moreover, it has been widely recognized that OHC is an important predictor for TC development and intensity (36–38), thereby underscoring the relevance of two-way air-sea interactions. Our current model setup with 1/10° ocean resolution allows us to study the TC sensitivity to greenhouse warming in the presence of such highly localized atmosphere-ocean coupling. To illustrate the upper ocean temperature response to the passage of a TC, we select a typical western North Pacific event that occurred between 6 July and 18 July in model year 124 of the PD simulation (Fig. 3). The TC first moves slowly with a translation speed of about 5 km hour^{-1} until it reaches 19°N. Thereafter, the translation speed accelerates to about 10 to 15 km hour^{-1} in the region between 20°N and 30°N. The maximum wind speed reaches 51 m s^{-1} around the well-resolved edge of the TC, which corresponds to a category 3 event based on the Saffir-Simpson scale for 1-min maximum sustained winds (Fig. 3A). The strong surface winds cool the upper ocean by up to 5°C preferentially along the right side of the track (Fig. 3E). This is where we observe also the strongest drop in OHC (Fig. 3F). The enhanced ocean response to the right of the TC track in the Northern Hemisphere occurs because the asymmetric wind stress provides nearly resonant forcing with inertial ocean currents that intensify entrainment of deeper colder water (35). The latent heat flux anomalies (Fig. 3C), which attain values of up to 1000 W m^{-2}, are stronger on the left side of the track, because negative SST anomalies are less pronounced there. The simulated precipitation shows the characteristic shape of spiraling rain bands (Fig. 3B).

To further examine TC-related changes in ocean thermodynamics, we identify SST cold wakes as the minimum SST anomaly within a period of 5 days after the TC passage and within a 200-km radius. The SST anomaly is calculated by subtracting the previous 14-day average. Overall, the simulated cold wake amplitudes are comparable to observational estimates (−5° to −10°C) (39), especially in the more stratified continental shelf regions (16, 39–41) (table S2). Cold wakes,
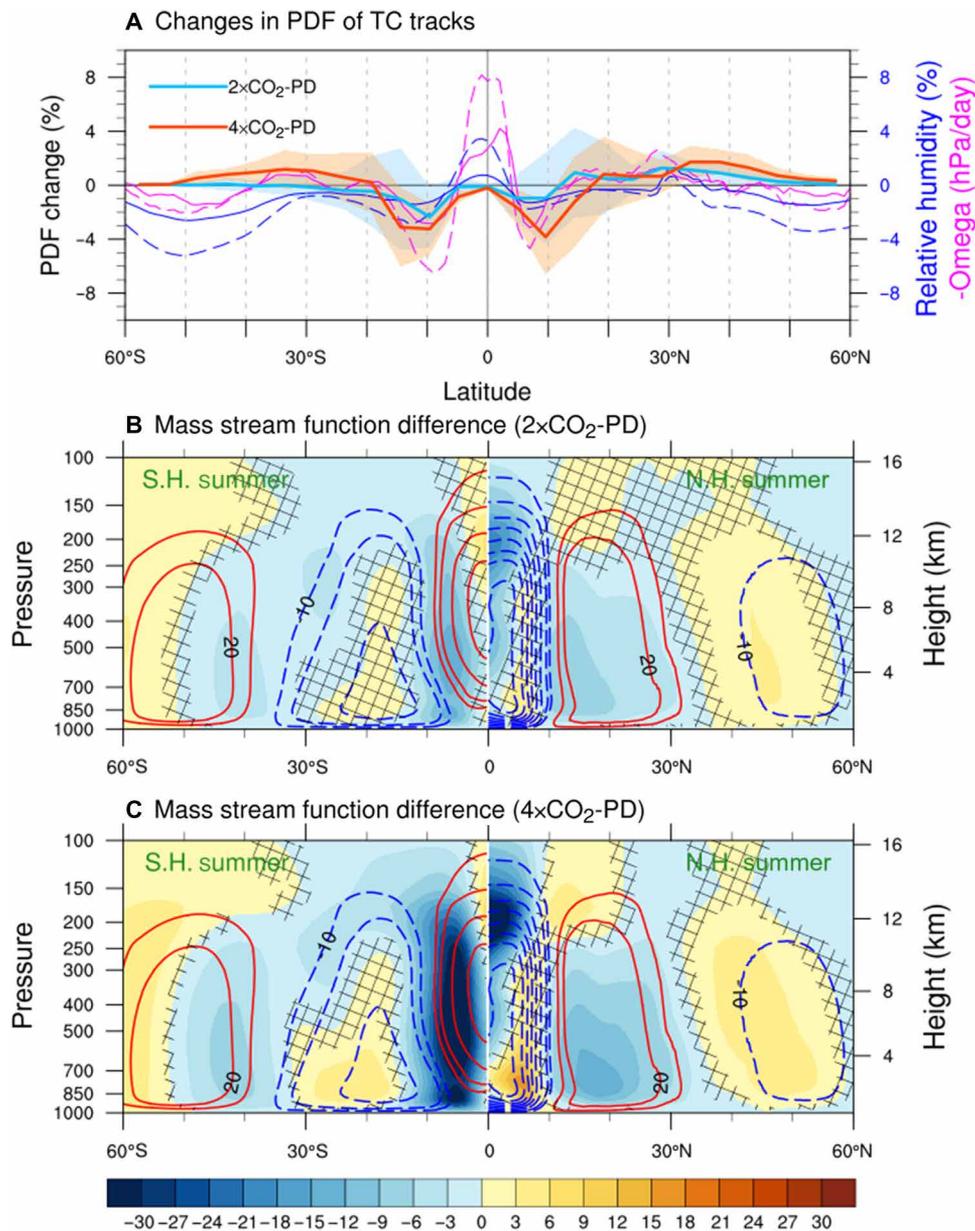
Fig. 2. Changes in latitudinal distribution of TC tracks and meridional overturning circulations. (**A**) Changes in the probability density distribution (PDF) of the TC tracks as a function of latitude in $2\times CO_2$ (light blue thick line) and $4\times CO_2$ (red thick line) conditions relative to PD. Annual and zonal mean relative humidity (%) at 700 hPa (blue thin lines) and vertical velocity (hectopascals per day) at 500 hPa (magenta thin lines) in $2\times CO_2$ (solid lines) and $4\times CO_2$ (dashed lines) conditions. For consistency, the vertical velocity is multiplied by -1. Shadings indicate 1 SD of the year-to-year PDFs for $2\times CO_2$ (blue) and $4\times CO_2$ (red) conditions. (**B** and **C**) Climatological summertime mass stream function in PD (contours) and changes in mass stream function (shading) in (B) $2\times CO_2$ and (C) $4\times CO_2$ experiments. Summer mean is computed over June to November for the Northern Hemisphere (N.H.) and December to May for the Southern Hemisphere (S.H.). Values that are not statistically significant at 95% confidence level are marked by black cross-hatching.

which can be found in the western North Pacific, southern Indian Ocean, eastern Pacific, and South Pacific, are most strongly pronounced for slowly propagating TCs over tropical and subtropical regions within 25°S to 25°N (Fig. 4A). We also find a secondary peak in cold wake amplitude around 40°N, where most of the storms have high translation speeds that can exceed 30 km hour^{-1} (Fig. 4B). The relationship between TC intensity and SST cooling at given TC translation speed conditions remains essentially unaltered for the $2\times CO_2$ and $4\times CO_2$ experiments (fig. S7). Our $4\times CO_2$ perturbation experi-

ment shows a discernable decrease in the annually accumulated tropical ocean surface cooling induced by TCs (Fig. 5), which can be attributed to the overall reduction in TC frequencies. An enhanced cold wake effect poleward of 40°N in the North Atlantic can be explained in terms of the simulated meridional extension of the TC tracks (Fig. 1, D and E).

The strongest TC-induced ocean cooling in our PD simulation attains extreme values of 15°C, which is larger than the observed maximum cooling (table S2). Previous studies have highlighted that
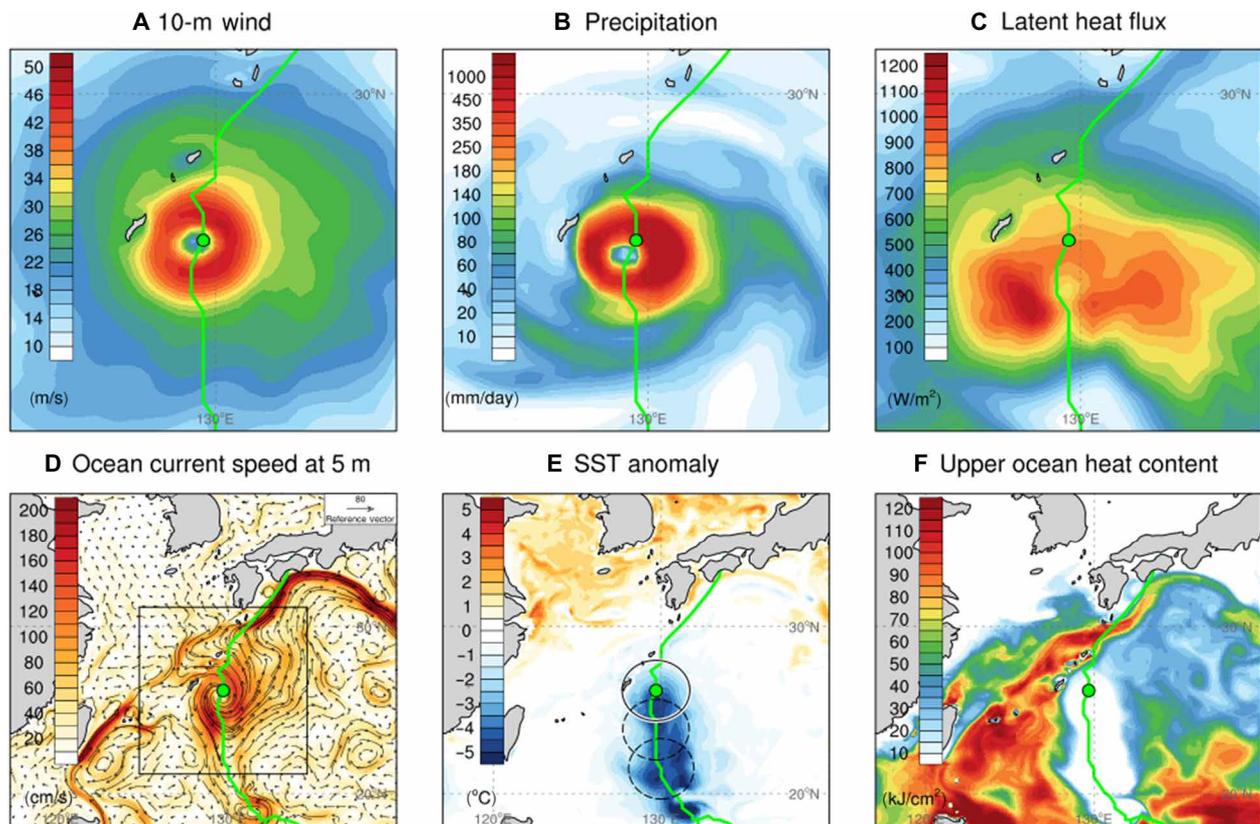
Fig. 3. Upper ocean response to the passage of a TC. A snapshot of (**A**) 10-m wind speed (meters per second), (**B**) precipitation (millimeters per day), (**C**) latent heat flux (watts per square meter), (**D**) ocean current (vector) and its speed (shading) (centimeters per second) at a depth of 5 m (centimeters per second), (**E**) SST (°C) anomaly, and (**F**) upper OHC (kilojoules per square centimeter) in response to a TC case passing over the western North Pacific. The SST anomaly is calculated by subtracting the previous 14-day average. Green line indicates the track of the selected TC, and green circle indicates the center of the storm. Black box in (D) denotes the zoomed-in area in (A) to (C). The circle with black solid line in (E) represents the 200-km boundary from the storm center that is used to calculate maximum SST cooling (i.e., cold wakes), whereas circles with black dashed line are those for storms at 24 and 48 hours before.

the standard parameterization of the drag coefficient in climate models tends to overestimate surface wind stress for high wind speeds (*42*, *43*). To avoid excessive ocean cooling for very high wind speeds, modifications to the drag coefficient parameterization have been proposed (*42*, *44*, *45*). In our simulations, the high wind speed adjustments have not been implemented, which may result in an overestimation of the TC cold wake effect. However, we emphasize that lower-resolution ocean models (*27*, *37*) show considerably weaker cold wakes, attaining strongest cooling of less than −1° to −2°C. In addition, our simulations show strong cooling near continental shelf regions only for slow-moving TCs. This indicates that the impacts of the oceanic resolution, background ocean stratification, and residence time of TCs play a larger role in determining the magnitude of SST cold wakes than the impact of drag coefficient adjustment for high wind speeds.

In our simulations, we find that TC-induced SST cooling is reduced in the southern Indian Ocean but not in the western North Pacific (Fig. 5). Since ocean thermal conditions are an important element to simulate realistic TC distributions (*46*, *47*), we further examine whether future changes in mixed-layer depth and the upper ocean vertical temperature gradient (SST minus temperature at 100-m depth) may influence TC-related air-sea coupling under CO_2 doubling and quadrupling conditions. The model simulates a future

mixed-layer depth shoaling and increase in the thermal stratification over the western North Pacific, which leads to favorable conditions for subsurface water entrainment (fig. S8), which can act as negative feedback to TC activity. The situation in the tropical Indian Ocean is the opposite. This effect may partly explain the weakening of the TC-induced SST cooling in the southern Indian Ocean. However, if the subsurface oceanic conditions influenced TC-related air-sea interactions, the cold wake amplitude per TC would also change. The cold wake histograms for the tropical South Indian Ocean and western North Pacific (fig. S9) show no discernible changes, suggesting that the change in TC-aggregated cooling (Fig. 5, B and C) can be explained simply in terms of TC density changes (Fig. 1) and is unrelated to changes in upper ocean thermal stratification.

Landfalling TCs
One of the key advantages of a mesoscale-resolving coupled model is its capability to resolve weather and climate processes in mountainous areas and along complex coastlines more accurately. To determine the future impact of TCs on heavily populated coastlines, we identify the TC landfall locations in PD, 2×CO_2, and 4×CO_2, as well as the corresponding changes in TC intensity and accumulated rainfall (Fig. 6). A landfalling TC occurs in our simulations when the land fraction in the TC area at a previous timestep is 0 and increases
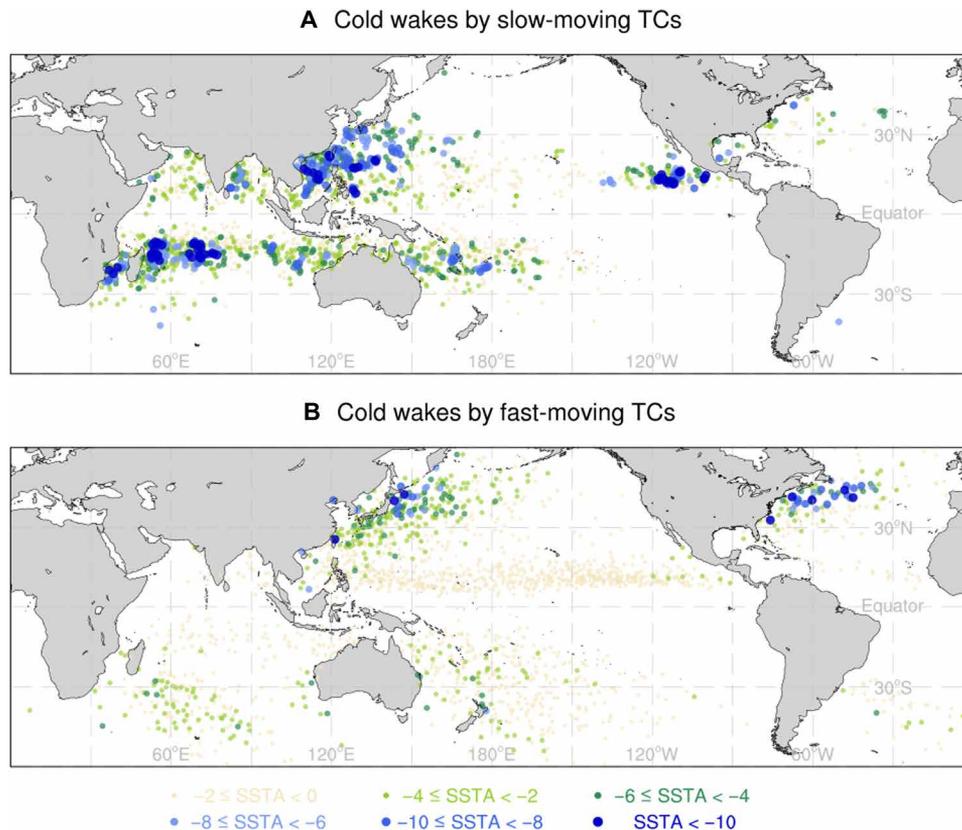
A Cold wakes by slow-moving TCs

B Cold wakes by fast-moving TCs

Fig. 4. Cold wakes and TC translation speeds. Global distribution of the TC-induced cold wakes by (**A**) slow-moving TCs and (**B**) fast-moving TCs in the PD simulation. Slow-moving TCs are defined as the TCs with translation speed lower than 10 km hour^{-1}. Fast-moving TCs are defined as those with speed greater than 30 km hour^{-1}. The cold wakes are identified as the minimum SST anomaly (SSTA) within a circle of 200-km radius (e.g., circles in Fig. 3E) during the next 5 days after the TC passage.

to greater than 0 in the next timestep. On the basis of this algorithm, the locations of landfalling TCs especially along the coastlines and many islands in the Indian Ocean and Western Pacific are well captured (Fig. 6B). The TC intensity and precipitation during landfall are calculated from the maximum wind speed within a 100-km circle from the storm center and the corresponding area-averaged precipitation. Averaged over the landfalling events, average simulated wind speed increases by 2.0 and 6.1% for the $2\times CO_2$ and $4\times CO_2$ experiments, respectively (fig. S10A). The projected changes in landfalling TC intensity are mainly due to the reduction in the number of weak TCs and an increase in category 3 to 5 TCs (Fig. 6E). The range of precipitation increase is 7 to 21% in $2\times CO_2$ and 17 to 47% in $4\times CO_2$, with most marked changes occurring in the median range over the distribution (Fig. 6F). The mean precipitation for subtropical landfalling TCs increases by 13.6 and 35.4% in $2\times CO_2$ and $4\times CO_2$, respectively. Even though TC frequencies are projected to decrease, our simulations document that landfalling TCs will be more impactful due to stronger winds and heavier precipitation. We note that the overall trends of TC intensity and precipitation diagnosed for landfalling TCs are qualitatively similar to those for all TCs including nonlandfalling events (fig. S10, C and D).

DISCUSSION

Previous studies (*2*, *4*, *27*) have emphasized the need to use coupled mesoscale-resolving global atmosphere/ocean models for projecting

the sensitivity of TCs to future climate change. Our results, which are based on one of the highest-resolution coupled global model simulations of long-term future climate change conducted so far, provide new insights into the mechanisms of future TC changes. Our model simulates a global reduction in TCs in response to greenhouse warming (Fig. 1, D and E, and table S1), thus adding an additional realistic coupled modeling perspective to an ongoing debate (*2*, *3*). The corresponding spatial pattern shows qualitative similarities with the observed trends (Fig. 1C), thereby lending further support to the suggestion of already emergent observational changes (*1*). The simulated TC reduction in large swaths of the tropics and an extension of the "forbidden near equatorial zone" in the western tropical Pacific (Fig. 6) can be explained by a weakening of the ascending branches of the summer Hadley cells in both hemispheres (Fig. 2) and associated changes in relative humidity and vertical motion (Fig. 2). The results are consistent with the recently identified observational linkage between Hadley cells and TC trends (*30*) and previous modeling studies that emphasize the role of large-scale tropical atmospheric changes as a controlling factor for future changes in TC development (*48–50*). The Hadley cell–induced suppression of TC densities in $4\times CO_2$ equatorward of 20° latitude (Fig. 2) includes a reduction in slow-moving TCs, which, in turn, leads to a weakening of the aggregated cold wake effect (Fig. 5) and a drop in TC-related ocean mixing.

The coupled model simulations presented here further support the robustness of the previously identified projected increase in the
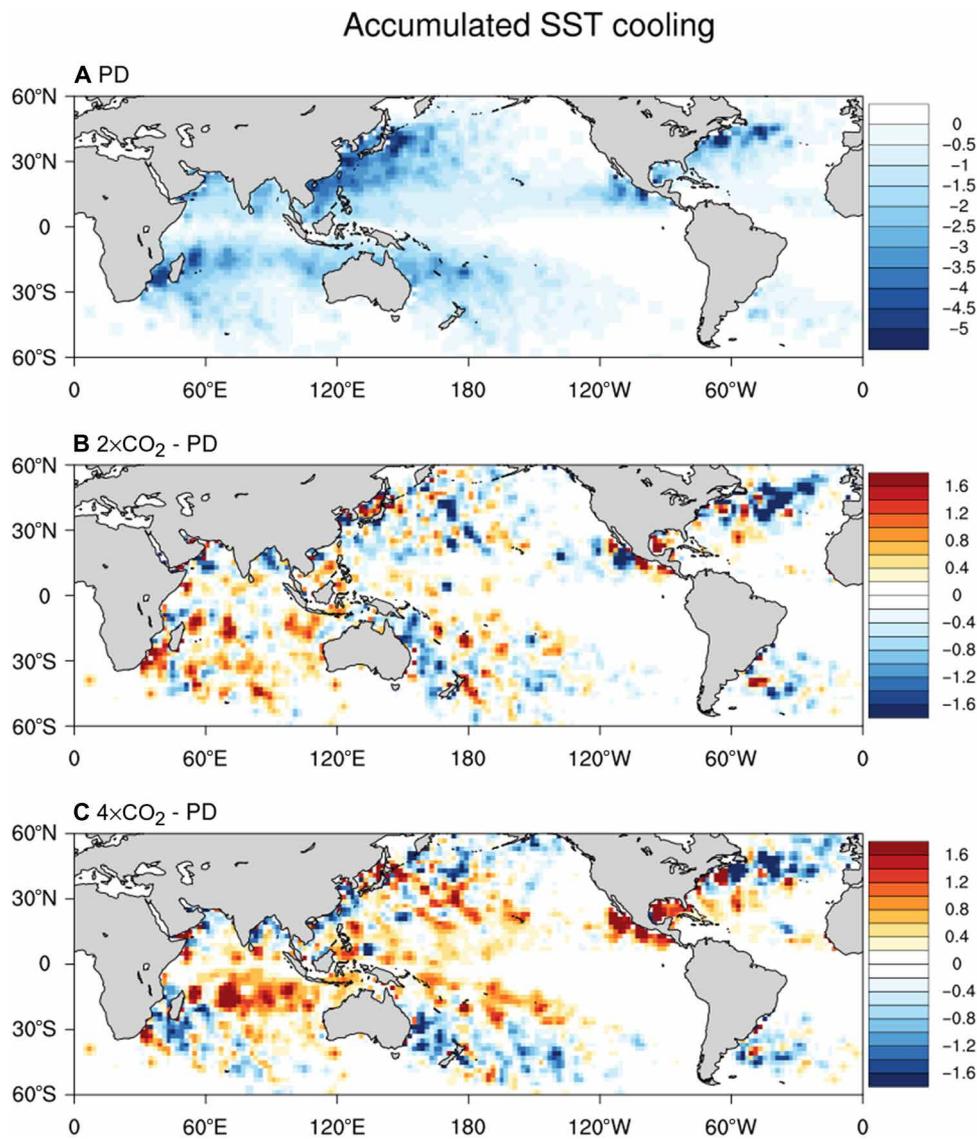
Accumulated SST cooling

Fig. 5. Accumulated SST cooling effect induced by TC activity. (**A**) Annually accumulated cooling due to TC passages in the PD experiment. The cooling effect is calculated by adding the SST anomaly within a circle of 200-km radius along the TC passages over a year. (**B** and **C**) Changes in SST cooling effect in (B) 2×CO_2 and (C) 4×CO_2 relative to PD. The patterns are interpolated to a 2 × 2 degree grid box. All fields are smoothed using a 9-point local average weighted by distance from the grid center.

global number of category 3 to 5 TCs (*3*, *10*) (Fig. 6E). However, the 2.0% increase in the magnitude of maximum wind speed from doubling CO_2 simulation (fig. S10) is at the lower end of the expected changes from the Intergovernmental Panel on Climate Change (IPCC) A1B future warming scenario (+2 to +11%) (*2*) and smaller than projections from the HiFLOR simulations (+3.2 to 9.0%) (*14*). The projected changes in landfalling TC intensity are nonlinear with a massive 150% increase in category 3 to 5 events occurring for the first CO_2 doubling (Fig. 6E), but no further change occurring between doubling and quadrupling. The statistical robustness of this saturation effect needs to be further explored in subsequent studies and for different model configurations.

One of the most robust projections (*14*, *51*) of future TC impacts is related to the largely thermodynamically controlled intensification of rainfall. This process is connected to an increased risk for coastal flooding. In the 2×CO_2 and 4×CO_2 experiments, the increase in tropical SST (averaged over 30°S to 30°N) by 1.8° and 3.7°C is accompanied by an increase in TC precipitation by 7.7 and 9.5% per degree warming, respectively. This increase slightly outpaces the rates expected from the thermodynamic Clausius-Clapeyron scaling (~7% °C^{-1}). This result is consistent with earlier reports suggesting that future TC precipitation is controlled by both the increases in environmental water vapor as well as storm intensity (*2*, *14*).

Even though our ultrahigh-resolution coupled simulations exhibit reduced tropical SST biases, in comparison with coarser-resolution coupled general circulation models, the mesoscale-resolving CESM1.2.2 PD simulation still exhibits substantial offsets in TC densities and tracks (fig. S5), in particular for North Atlantic hurricanes. A more detailed analysis is necessary to ascertain the role of biases in convection and in the representation of easterly waves and tropical
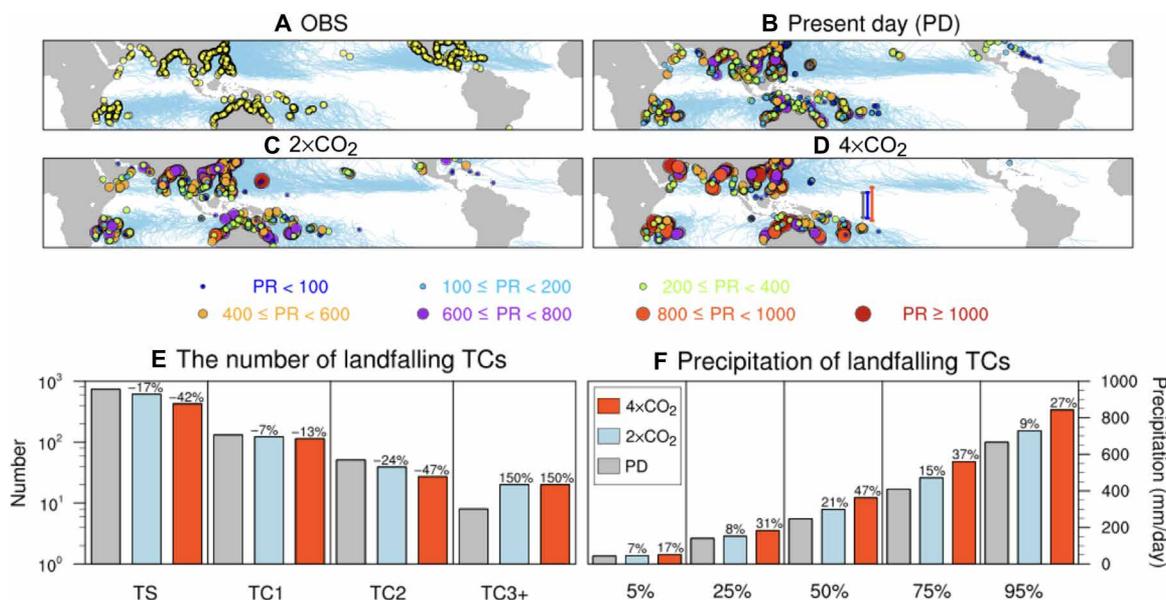
Fig. 6. Locations, precipitation, and intensity of landfalling TCs. (**A** to **D**) TC tracks (light blue) and landfalling locations (yellow or colored circles) from (A) observation, (B) PD, (C) 2×CO$_2$, and (D) 4×CO$_2$ simulations. Colors in (B) to (D) indicate different range of precipitation (PR) averaged over a circle of 100-km radius from the storm center. (**E**) The number of landfalling TCs for each category from tropical storm (TS) to TC greater than category 3 (TC3+) based on the Saffir-Simpson scale in PD (gray), 2×CO$_2$ (blue), and 4×CO$_2$ (red) conditions. (**F**) Precipitation (millimeters per day) by the landfalling TCs at each percentile of 5, 25, 50 (median), 75, and 95%, respectively. Numbers above the bars indicate relative changes in the (E) TC number and (F) precipitation compared with PD values. To remove the impact of extratropical storms, landfalling TCs within 30°S to 30°N are considered. Vertical bars in (D) denote the "forbidden near equatorial zone" defined as a longitudinal average of the genesis location nearest to the equator between 30°E and 180°E for PD (gray), 2×CO$_2$ (blue), and 4×CO$_2$ (red), respectively.

Atlantic SST errors (fig. S2). A viable approach to overcome the potential effects of SST biases on TC genesis and tracks under PD condition would be to use SST nudging techniques that tie the simulated SST closer to the observations (*3*). However, it remains unclear to what extent such methods can be applied for stronger CO$_2$ perturbations, such as for CO$_2$ quadrupling.

Summarizing, our mesoscale-resolving coupled CO$_2$ perturbation experiments confirm several previously suggested elements of the TC response to greenhouse warming. Furthermore, we identify a number of new important features, such as the robust reduction in aggregated TC ocean cooling and associated mixing equatorward of 20° latitude (Fig. 5), as well as saturation in wind intensity for CO$_2$ quadrupling (Fig. 6E) that highlights the added value of improved representations of mesoscale air-sea coupling and coastal and topographic processes.

MATERIALS AND METHODS
Model and computational descriptions
In the present study, the CESM1.2.2 is used to perform fully coupled ultrahigh-resolution simulations. The atmosphere component is the CAM5 with a spectral element dynamic core at a horizontal resolution of around 0.25° and 30 vertical layers. CAM5 is able to capture TCs and observed behavior of global accumulated cyclone energy, albeit with large basin-to-basin differences in TC climatologies (fig. S5) (*7*). The ocean component of CESM is the POP2, which is configured with a horizontal resolution of 0.1° (decreasing from 11 km at the equator to 2.5 km at high latitudes) and 62 vertical levels. The land model is the Community Land Model version 4 (CLM4) and the sea-ice component is the Community Ice Code

version 4 (CICE4). The prognostic carbon-nitrogen cycle component was turned off in our simulations. The configuration for our PD experiment is very similar to the one used in an earlier study (*21*), except that we adjusted some elements of the convection scheme to improve our PD representation of the El Niño–Southern Oscillation. The ultrahigh-resolution CESM1.2.2 shows a substantial mean-state bias reduction in SST (fig. S2) and is capable of capturing localized small-scale phenomena such as air-sea interactions over ocean frontal zones, mesoscale ocean eddies (fig. S4), and atmospheric extremes including eye-walled TCs and convective systems generated by the Rocky Mountains (*21*).

We conduct three experiments with different levels of fixed greenhouse gas conditions: (i) PD with a CO$_2$ concentration of 367 ppm, (ii) CO$_2$ doubling (2×CO$_2$, 734 ppm), and (iii) CO$_2$ quadrupling (4×CO$_2$, 1468 ppm). All other greenhouse gas and aerosol concentrations have been kept at PD levels. The PD simulation was initialized from a quasi-equilibrated climate state (*21*) and was then integrated for another 140 years. The doubling and quadrupling CO$_2$ forcing experiments were branched off from year 71 of the PD experiment and integrated for 100 years each. For the TC analysis, we focus on the better equilibrated last 20 years of each simulation. Unless otherwise stated, all other variables used in the main text focus on the last 20 years of each simulation.

TC detection and track
TCs are detected and tracked by adopting (with some minor adjustments) a recently proposed method (*7*). For our detection, we use six-hourly instantaneous surface pressure, 10-m wind speed, and surface vorticity. First, we identify candidate lows by calculating local surface pressure anomaly minima (threshold: lower than −3 hPa).

Surface pressure anomalies (PS') are obtained by subtracting surface pressure from a 14-day retrospective mean $PS'_t = PS_t - [PS]_{(-14d, -1d)}$, where the square bracket denotes a time average. If the maximum 10-m wind speed within a 100-km radius from the local pressure minimum does not exceed 10 m s^{-1}, the low is discarded. After finding candidate lows at all time steps, we use tracking over six-hourly intervals. The next track location at $t + 6$ hours is chosen simply as the nearest low to the original low at time t. If another low is located within a 400-km radius circle, the track is continued. At subsequent time step ($t + 12$ hours), the low closest to the location that is extrapolated between t and $t + 6$ hours is chosen to be the next track. If no other low is located within a 400-km radius circle, the track is terminated. This scheme is almost the same as the original method (7), except they use three-hourly instantaneous data, 200-km radius for tracks, and 50-km radius for wind speed. To avoid multiple counting of a single storm, we additionally remove any duplicated tracks and keep the track that the one started earliest. In addition, if the maximum of wind speed along the track never reaches 17 m s^{-1}, which is the threshold for a tropical storm on the Saffir-Simpson scale, and the duration of the storm is less than 2 days, the track is also eliminated. Last, we impose a threshold value of 0.00145 s^{-1} for surface vorticity magnitude along the track to obtain global TC numbers of around 85 per year, similar to the observations.

Translation speed

The translation speed is calculated on the basis of the great circle distance of two points between that at 6 hours before and 6 hours after the current location and then divided by 12 hours. Translation speed at initial and final positions is calculated using the two neighboring forward and backward positions, respectively.

Upper OHC

Following a previous study (52), the OHC is defined here as

$$\text{OHC} = \rho_0 C_p \int_{Z26}^{0} [T(z) - 26] \, dz \qquad (1)$$

where ρ_0 is the sea water density ($\rho_0 = 1025$ kg m^{-3}), C_p is the ocean heat capacity ($C_p = 4.0 \times 10^3$ J kg^{-1} °C^{-1}), and $T(z)$ is the ocean temperature as a function of depth z down to the 26°C isotherm, Z_{26}. The reference depth Z_{26} is the climatological depth during the respective TC season. For the TC case over the western North Pacific (Fig. 3), the climatological Z_{26} is calculated during June to October. Note that the existence of a 26°C isotherm is a necessary condition for TC formation.

SUPPLEMENTARY MATERIALS

Supplementary material for this article is available at http://advances.sciencemag.org/cgi/content/full/6/51/eabd5109/DC1

REFERENCES AND NOTES

1. H. Murakami, T. L. Delworth, W. F. Cooke, M. Zhao, B. Xiang, P.-C. Hsu, Detected climatic change in global distribution of tropical cyclones. *Proc. Natl. Acad. Sci. U.S.A.*, 10706–10714 (2020).
2. T. R. Knutson, J. L. McBride, J. Chan, K. Emanuel, G. Holland, C. Landsea, I. Held, J. P. Kossin, A. K. Srivastava, M. Sugi, Tropical cyclones and climate change. *Nat. Geosci.* **3**, 157–163 (2010).
3. G. A. Vecchi, T. L. Delworth, H. Murakami, S. D. Underwood, A. T. Wittenberg, F. Zeng, W. Zhang, J. W. Baldwin, K. T. Bhatia, W. Cooke, J. He, S. B. Kapnick, T. R. Knutson, G. Villarini, K. van der Wiel, W. Anderson, V. Balaji, J.-H. Chen, K. W. Dixon, R. Gudgel, L. M. Harris, L. Jia, N. C. Johnson, S.-J. Lin, M. Liu, C. H. J. Ng, A. Rosati, J. A. Smith, X. Yang,

Tropical cyclone sensitivities to CO$_2$ doubling: Roles of atmospheric resolution, synoptic variability and background climate changes. *Climate Dynam.* **53**, 5999–6033 (2019).
4. H. Li, R. L. Sriver, Effects of ocean grid resolution on tropical cyclone-induced upper ocean responses using a global ocean general circulation model. *J. Geophys. Res. Oceans* **121**, 8305–8319 (2016).
5. H. Li, R. L. Sriver, Impact of air–sea coupling on the simulated global tropical cyclone activity in the high-resolution Community Earth System Model (CESM). *Climate Dynam.* **53**, 3731–3750 (2019).
6. E. Scoccimarro, P. G. Fogli, K. A. Reed, S. Gualdi, S. Masina, A. Navarra, Tropical cyclone interaction with the ocean: The role of high-frequency (subdaily) coupled processes. *J. Climate* **30**, 145–162 (2017).
7. J. T. Bacmeister, M. F. Wehner, R. B. Neale, A. Gettelman, C. Hannay, P. H. Lauritzen, J. M. Caron, J. E. Truesdale, Exploratory high-resolution climate simulations using the community atmosphere model (CAM). *J. Climate* **27**, 3073–3099 (2014).
8. K. A. Reed, J. T. Bacmeister, N. A. Rosenbloom, M. F. Wehner, S. C. Bates, P. H. Lauritzen, J. E. Truesdale, C. Hannay, Impact of the dynamical core on the direct simulation of tropical cyclones in a high-resolution global model. *Geophys. Res. Lett.* **42**, 3603–3608 (2015).
9. H. Murakami, R. Mizuta, E. Shindo, Future changes in tropical cyclone activity projected by multi-physics and multi-SST ensemble experiments using the 60-km-mesh MRI-AGCM. *Climate Dynam.* **39**, 2569–2584 (2012).
10. H. Murakami, Y. Wang, H. Yoshimura, R. Mizuta, M. Sugi, E. Shindo, Y. Adachi, S. Yukimoto, M. Hosaka, S. Kusunoki, T. Ose, A. Kitoh, Future changes in tropical cyclone activity projected by the new high-resolution MRI-AGCM. *J. Climate* **25**, 3237–3260 (2012).
11. J. T. Bacmeister, K. A. Reed, C. Hannay, P. Lawrence, S. Bates, J. E. Truesdale, N. Rosenbloom, M. Levy, Projected changes in tropical cyclone activity under future warming scenarios using a high-resolution climate model. *Clim. Change* **146**, 547–560 (2018).
12. M. F. Wehner, K. A. Reed, B. Loring, D. Stone, H. Krishnan, Changes in tropical cyclones under stabilized 1.5 and 2.0 °C global warming scenarios as simulated by the Community Atmospheric Model under the HAPPI protocols. *Earth Syst. Dynam.* **9**, 187–195 (2018).
13. M. J. Roberts, P. L. Vidale, M. S. Mizielinski, M.-E. Demory, R. Schiemann, J. Strachan, K. Hodges, R. Bell, J. Camp, Tropical cyclones in the UPSCALE ensemble of high-resolution global climate models*. *J. Climate* **28**, 574–596 (2015).
14. M. Liu, G. A. Vecchi, J. A. Smith, T. R. Knutson, Causes of large projected increases in hurricane precipitation rates with global warming. *npj Clim. Atmos. Sci.* **2**, 38 (2019).
15. H.-S. Kim, G. A. Vecchi, T. R. Knutson, W. G. Anderson, T. L. Delworth, A. Rosati, F. Zeng, M. Zhao, Tropical cyclone simulation and response to CO$_2$ doubling in the GFDL CM2.5 high-resolution coupled climate model. *J. Climate* **27**, 8034–8054 (2014).
16. T.-L. Chiang, C.-R. Wu, L.-Y. Oey, Typhoon Kai-Tak: An ocean's perfect storm. *J. Phys. Oceanogr.* **41**, 221–233 (2011).
17. M.-S. Park, R. L. Elsberry, P. A. Harr, Vertical wind shear and ocean heat content as environmental modulators of Western North Pacific tropical cyclone intensification and decay. *Trop. Cyclone Res. Rev.* **1**, 448–457 (2012).
18. K. E. Trenberth, L. Cheng, P. Jacobs, Y. Zhang, J. Fasullo, Hurricane Harvey links to ocean heat content and climate change adaptation. *Earths Future* **6**, 730–744 (2018).
19. R. L. Sriver, M. Huber, Observational evidence for an ocean heat pump induced by tropical cyclones. *Nature* **447**, 577–580 (2007).
20. C. M. Zarzycki, Tropical cyclone intensity errors associated with lack of two-way ocean coupling in high-resolution global simulations. *J. Climate* **29**, 8589–8610 (2016).
21. R. J. Small, J. Bacmeister, D. Bailey, A. Baker, S. Bishop, F. Bryan, J. Caron, J. Dennis, P. Gent, H.-m. Hsu, M. Jochum, D. Lawrence, E. Muñoz, P. diNezio, T. Scheitlin, R. Tomas, J. Tribbia, Y.-h. Tseng, M. Vertenstein, A new synoptic scale resolving global climate simulation using the Community Earth System Model. *J. Adv. Model. Earth Syst.* **6**, 1065–1094 (2014).
22. P. M. Caldwell, A. Mametjanov, Q. Tang, L. P. Van Roekel, J.-C. Golaz, W. Lin, D. C. Bader, N. D. Keen, Y. Feng, R. Jacob, M. E. Maltrud, A. F. Roberts, M. A. Taylor, M. Veneziani, H. Wang, J. D. Wolfe, K. Balaguru, P. Cameron-Smith, L. Dong, S. A. Klein, L. R. Leung, H.-Y. Li, Q. Li, X. Liu, R. B. Neale, M. Pinheiro, Y. Qian, P. A. Ullrich, S. Xie, Y. Yang, Y. Zhang, K. Zhang, T. Zhou, The DOE E3SM coupled model version 1: Description and results at high resolution. *J. Adv. Model. Earth Syst.* **11**, 4095–4146 (2019).
23. J. L. McClean, D. C. Bader, F. O. Bryan, M. E. Maltrud, J. M. Dennis, A. A. Mirin, P. W. Jones, Y. Y. Kim, D. P. Ivanova, M. Vertenstein, J. S. Boyle, R. L. Jacob, N. Norton, A. Craig, P. H. Worley, A prototype two-decade fully-coupled fine-resolution CCSM simulation. *Ocean Model.* **39**, 10–30 (2011).
24. M. J. Widlansky, A. Timmermann, K. Stein, S. McGregor, N. Schneider, M. H. England, M. Lengaigne, W. Cai, Changes in South Pacific rainfall bands in a warming climate. *Nat. Clim. Change* **3**, 417–423 (2013).
25. A. Bellucci, S. Gualdi, A. Navarra, The double-ITCZ syndrome in coupled general circulation models: The role of large-scale vertical circulation regimes. *J. Climate* **23**, 1127–1145 (2010).
26. J.-L. Lin, The double-ITCZ problem in IPCC AR4 coupled GCMs: Ocean–atmosphere feedback analysis. *J. Climate* **20**, 4497–4525 (2007).

27. H. Murakami, G. A. Vecchi, S. Underwood, T. L. Delworth, A. T. Wittenberg, W. G. Anderson, J.-H. Chen, R. G. Gudgel, L. M. Harris, S.-J. Lin, F. Zeng, Simulation and prediction of category 4 and 5 hurricanes in the high-resolution GFDL HiFLOR coupled climate model. *J. Climate* **28**, 9058–9079 (2015).

28. G. J. Huffman, D. T. Bolvin, E. J. Nelkin, D. B. Wolff, R. F. Adler, G. Gu, Y. Hong, K. P. Bowman, E. F. Stocker, The TRMM multisatellite precipitation analysis (TMPA): Quasi-global, multiyear, combined-sensor precipitation estimates at fine scales. *J. Hydrometeorol.* **8**, 38–55 (2007).

29. K. R. Knapp, M. C. Kruk, D. H. Levinson, H. J. Diamond, C. J. Neumann, The International Best Track Archive for Climate Stewardship (IBTrACS): Unifying tropical cyclone data. *Bull. Am. Meteorol. Soc.* **91**, 363–376 (2010).

30. S. Sharmila, K. J. E. Walsh, Recent poleward shift of tropical cyclone formation linked to Hadley cell expansion. *Nat. Clim. Change* **8**, 730–736 (2018).

31. J. Studholme, S. Gulev, Concurrent changes to Hadley circulation and the meridional distribution of tropical cyclones. *J. Climate* **31**, 4367–4389 (2018).

32. I. M. Held, M. Zhao, The response of tropical cyclone statistics to an increase in CO_2 with fixed sea surface temperatures. *J. Climate* **24**, 5353–5364 (2011).

33. L. Bengtsson, K. I. Hodges, E. Roeckner, Storm tracks and climate change. *J. Climate* **19**, 3518–3543 (2006).

34. I.-J. Moon, S.-H. Kim, J. C. L. Chan, Climate change and tropical cyclone trend. *Nature* **570**, E3–E5 (2019).

35. J. F. Price, Upper ocean response to a hurricane. *J. Phys. Oceanogr.* **11**, 153–175 (1981).

36. K. A. Emanuel, Thermodynamic control of hurricane intensity. *Nature* **401**, 665–669 (1999).

37. I. D. Lloyd, G. A. Vecchi, Observational evidence for oceanic controls on hurricane intensity. *J. Climate* **24**, 1138–1153 (2011).

38. E. M. Vincent, K. A. Emanuel, M. Lengaigne, J. Vialard, G. Madec, Influence of upper ocean stratification interannual variability on tropical cyclones. *J. Adv. Model. Earth Syst.* **6**, 680–699 (2014).

39. E. A. D'Asaro, P. G. Black, L. R. Centurioni, Y.-T. Chang, S. S. Chen, R. C. Foster, H. C. Graber, P. Harr, V. Hormann, R.-C. Lien, I.-I. Lin, T. B. Sanford, T.-Y. Tang, C.-C. Wu, Impact of typhoons on the ocean in the Pacific. *Bull. Am. Meteorol. Soc.* **95**, 1405–1418 (2014).

40. J.-H. Park, D.-E. Yeo, K. Lee, H. Lee, S.-W. Lee, S. Noh, S. Kim, J. Shin, Y. Choi, S. Nam, Rapid decay of slowly moving typhoon Soulik (2018) due to interactions with the strongly stratified Northern East China sea. *Geophys. Res. Lett.* **46**, 14595–14603 (2019).

41. A. Wada, T. Uehara, S. Ishizaki, Typhoon-induced sea surface cooling during the 2011 and 2012 typhoon seasons: Observational evidence and numerical investigations of the sea surface cooling effect using typhoon simulations. *Prog Earth Planet Sci* **1**, 11 (2014).

42. I.-J. Moon, I. Ginis, T. Hara, B. Thomas, A physics-based parameterization of air–sea momentum flux at high wind speeds and its impact on hurricane intensity predictions. *Mon. Weather Rev.* **135**, 2869–2878 (2007).

43. M. D. Powell, P. J. Vickery, T. A. Reinhold, Reduced drag coefficient for high wind speeds in tropical cyclones. *Nature* **422**, 279–283 (2003).

44. M. R. Bueti, I. Ginis, L. M. Rothstein, S. M. Griffies, Tropical cyclone–induced thermocline warming and its regional and global impacts. *J. Climate* **27**, 6978–6999 (2014).

45. H. Li, R. L. Sriver, Tropical cyclone activity in the high-resolution community earth system model and the impact of ocean coupling. *J. Adv. Model. Earth Syst.* **10**, 165–186 (2018).

46. T. Ogata, R. Mizuta, Y. Adachi, H. Murakami, T. Ose, Effect of air-sea coupling on the frequency distribution of intense tropical cyclones over the northwestern Pacific. *Geophys. Res. Lett.* **42**, 10415–410421 (2015).

47. T. Ogata, R. Mizuta, Y. Adachi, H. Murakami, T. Ose, Atmosphere-ocean coupling effect on intense tropical cyclone distribution and its future change with 60 km-AOGCM. *Sci. Rep.* **6**, 29800 (2016).

48. M. Sugi, H. Murakami, J. Yoshimura, On the mechanism of tropical cyclone frequency changes due to global warming. *J. Meteorol. Soc. Jpn.* **90A**, 397–408 (2012).

49. M. Sugi, A. Noda, N. Sato, Influence of the global warming on tropical cyclone climatology: An experiment with the JMA global model. *J. Meteorol. Soc. Jpn.* **80**, 249–272 (2002).

50. S. S. Bell, S. S. Chand, K. J. Tory, A. J. Dowdy, C. Turville, H. Ye, Projections of southern hemisphere tropical cyclone track density using CMIP5 models. *Climate Dynam.* **52**, 6065–6079 (2019).

51. K. Yoshida, M. Sugi, R. Mizuta, H. Murakami, M. Ishii, Future changes in tropical cyclone activity in high-resolution large-ensemble simulations. *Geophys. Res. Lett.* **44**, 9910–9917 (2017).

52. D. F. Leipper, D. Volgenau, Hurricane heat potential of the gulf of Mexico. *J. Phys. Oceanogr.* **2**, 218–224 (1972).

53. J. W. Hurrell, J. J. Hack, D. Shea, J. M. Caron, J. Rosinski, A new sea surface temperature and sea ice boundary dataset for the Community Atmosphere Model. *J. Climate* **21**, 5145–5153 (2008).

54. N. Ducet, P. Y. Le Traon, G. Reverdin, Global high-resolution mapping of ocean circulation from TOPEX/Poseidon and ERS-1 and -2. *J. Geophys. Res. Oceans* **105**, 19477–19498 (2000).

Citation: J.-E. Chu, S.-S. Lee, A. Timmermann, C. Wengel, M. F. Stuecker, R. Yamaguchi, Reduced tropical cyclone densities and ocean effects due to anthropogenic greenhouse warming. *Sci. Adv.* **6**, eabd5109 (2020).

ScienceAdvances

Reduced tropical cyclone densities and ocean effects due to anthropogenic greenhouse warming

Jung-Eun Chu, Sun-Seon Lee, Axel Timmermann, Christian Wengel, Malte F. Stuecker and Ryohei Yamaguchi